Available online at www.sciencedirect.com

ScienceDirect

Procedia CIRP 104 (2021) 839–844

www.elsevier.com/locate/procedia

54th CIRP Conference on Manufacturing Systems

# Parametric compensation scheme for increasing the geometrical accuracy of lattice structures in medical implants produced by powder bed fusion

Max Horn[a,*], Lukas Koch[a], Mario Schafnitzel[a], Matthias Schmitt[a], Georg Schlick[a], Johannes Schilp[a,b], Gunther Reinhart[a,c]

[a]*Fraunhofer Institute for Casting, Composite and Processing Technology IGCV, Am Technologiezentrum 10, 86159 Augsburg, Germany*
[b]*University of Augsburg, Chair of Digital Manufacturing, Faculty of Applied Computer Sience, Eichleitnerstr. 30, 86159 Augsburg, Germany*
[c]*Technical University of Munich, Institute for Machine Tools and Industrial Management, Boltzmannstr. 15, 85748 Garching n. Munich, Germany*

* Corresponding author. Tel.: +49 821 90678-187. *E-mail address:* max.horn@igcv.fraunhofer.de

**Abstract**

Powder bed fusion of metals by laser beam enables the production of porous lattice structures that facilitate bone ingrowth and the vascularization of medical implants. Comprehensive implementation is currently limited by the medium reproducibility of porous structures with insufficient dimensional accuracy. Therefore strategies for minimizing geometrical mismatch and roughness are investigated by way of experiment. A parametric compensation scheme that takes into account the melt pool depth of the struts' downskins in reducing the geometric mismatch between as-designed and as-built lattice structures is proposed. Build angles of 10° with respect to the platform were created without support structures.



*Keywords:* Additive manufacturing; power bed fusion; laser beam; lattice structures; medical implants; stainless steel; 316L; overhang angle; thin struts;

## 1. Introduction

### *1.1. Laser powder bed fusion of medical implants*

Of all the additive manufacturing (AM) solutions in current use, powder bed fusion (PBF) by laser beam (LB) is the processing technique most commonly used with metals (M) [1]. The so-called PBF-LB/M process is especially suited for the production of parts of great geometrical complexity in small lot sizes and in a large variety [2, 3], a good example being custom medical implants [4]. An additional benefit of PBF-LB/M is its suitability for creating parts of graded porosity, which enables the Young's modulus of metals to be approximated to that of human bone. This is necessary to reduce the effect of stress shielding [5]. Lattice structures of defined porosity enable bone tissue ingrowth, or osseointegration with long-term implants [5–7]. A lattice structure can be described as a periodical order of unit cells that inhibit a structure of interconnected struts or surfaces [8], which makes them the primary choice for osseointegration in orthopedic implants [5]. Lattice structures are especially suited for PBF-LB/M, as conventional manufacturing techniques are uneconomic and unable to yield the desired component complexities [4, 9]. With PBF-LB/M, titanium alloys, cobalt-chromium alloys, and stainless steels are the predominant materials used in the production of medical implants, thanks to their high biocompatibility and low corrosiveness [7, 10–12]. Parts produced must be free of lightly sintered or loosely attached particles on the surface of the implants that could otherwise be released into the body [13]. The implant material must not contain any open porosity, as this would promote corrosion, resulting in material pitting and cracking [13]. To enable osseointegration, implants must also display both a defined surface roughness in order to secure cell attachment [7] and a certain level of dimensional accuracy in terms of pore size and porosity to secure the exchange of nutrition, oxygen and waste products for bone cells through diffusion [5, 6, 8]. As described by Bagheri et al., PBF-LB/M is currently

2212-8271 
10.1016/j.procir.2021.11.141

deficient in all of these aspects and fails to reproduce cellular geometries with the required degree of fidelity and accuracy [14]. One reason for these shortcomings is the staircase effect, which creates a dimensional mismatch leading to an excessive adherence of particles from the surrounding powder bed [15, 16]. Furthermore, overhang angles of less than 45° with respect to the build platform are generally supported during the production process to prevent warping and heat accumulation [15]. The removal of such support structures during post-processing is, however, impossible in the case of metallic cellular scaffolds. This limitation of 45° is critical, as structures that facilitate unit cells, such as those with the form of a tetrahedron or diamond, which indicate good in-vivo osseointegration, have smaller overhang angles [16]. In addition, the dissipation of the heat from the melting process differs due to the absence of support structures and the low volume of solidified material [17]. As a result of this, melt pool sizes grow and struts tend to thicken. Strut diameter deviations increase with smaller overhang angles [14, 17] and have been shown to be larger than 60% [14]. Heat accumulation is especially high on the downside of the struts, which leads to increased sintering of particles from the powder bed to the downskin of the parts [17, 18]. Advancements in build strategies (e. g., [17, 19, 20]) and compensation schemes (e. g., [14]) yield significant improvements in lattice structure quality but still fail to produce the desired level of fidelity and accuracy, especially for build angles below 40° [14].

### *1.2. Problem statement and approach*

The potential for producing lattice structures for custom medical implants using PBF-LB/M has not yet been fully exploited. Single struts of metallic cellular scaffolds lack dimensional accuracy and display increased downskin roughness. This study addresses this problem by suggesting a novel scanning strategy based on the actual melt pool dimensions approximated by normalized enthalpy at melting to align melt pools such that heat conduction is improved and the dissipation of thermal energy increased.

## 2. Materials and methods

### *2.1. Normalized enthalpy at melting*

Volumetric energy density (VED), as suggested by Meiners with reference to PBF-LB/M [21], is the most common metric used to compare components produced by PBF-LB/M with varying process parameters [22]. However, VED fails to accurately describe properties such as track shape and the resultant melting mode [22]. For this reason, the model proposed by King et al. which is based on previous work by Hann et al., was chosen for the present study [23, 24]. Research has shown that welding data from different machines and materials can be represented by a single curve, since the ratio between melt pool depth $d$ and beam spot size $\sigma$ is a function of the ratio of deposited energy density $\Delta H$ to enthalpy at melting $h_s$ [22] only. As this model considers both known welding modes – conduction mode and keyhole mode – it enables more accurate prediction of melt pool dimensions [22]. Normalized enthalpy is calculated with the following equation [24]:

$$\frac{\Delta H}{h_s} = \frac{AP_L}{h_s\sqrt{\pi D v \sigma^3}} \quad (1)$$

with absorptivity of the material $A$, laser power $P_L$, thermal diffusivity of the material $D$, and scanning velocity $v$. Enthalpy at melting, in turn, is described as [25]:

$$h_s = \rho c(T_m - T_0) \quad (2)$$

with material density $\rho$, specific heat capacity $c$, the material's melting temperature $T_m$, and its initial temperature $T_0$. This study uses the criterion suggested by King et al. to assign measured melt pools of single line tracks to the respective welding modes. Thus, keyhole-mode laser welding takes place when the depth of the melt pool is greater than the melt pool half-width [23].

### *2.2. Manufacturing and analysis of specimens*

With consideration for the application of spinal cages and the potential of low-cost manufacturing, stainless steel 316L (X2CrNiMo17-12-2, or 1.4404) was selected for all experiments due to its corrosion resistance and other mechanical properties [26]. The gas-atomized powder was supplied by Nanoval GmbH & Co. KG and had a particle size distribution of $d_{10,3}$ = 14 µm, $d_{50,3}$ = 25 µm, and $d_{90,3}$ = 43 µm, as measured by laser diffraction analysis and with wet dispersion according to ISO 13320 facilitated by a Mastersizer 3000 [27]. The powder was processed by an SLM 125$^{HL}$ PBF-LB machine with an ytterbium-fiber laser. The laser spot size was 63.7 µm, measured pursuant to DIN EN ISO 11146-2[28]. All specimens were produced at a build platform temperature of 200 °C, with a hatch distance of 100 µm and a nominal layer thickness of 30 µm; other scanning parameters varied (See Section 3). Preparation of machine data was done with a Materialise NV module for Siemens NX 12.

To quantify the melt pool dimensions, single line experiments were conducted with test specimens of dimensions (x, y, z) 10 x 5 x 5 mm$^3$. Three continuous line scanning tracks were deposited at the top of each specimen. The specimens were cut vertically and perpendicularly to the single line tracks, etched in a 3:1 $HCl/HNO_3$ solution for 120 s and analyzed with an Olympus BX53M optical microscope. Fig. 1 shows a scheme of the specimens with two example melt pools. To study the influence of the build angle, struts of a length of 5 mm with different overhang angles were produced using specimens as shown in Fig. 2 (a). To meet the osseointegration requirements, a nominal diameter of 500 µm was chosen for all struts. The dimensional accuracy and roughness of the struts was analyzed with an optical microscope using a Matlab algorithm to binarize the image, separate the background from the structure of interest using the watershed algorithm, map the contour of the structure separated by the Matlab function *bwboundaries* to x/y coordinates and calculate the distance between corresponding x-values for a certain y-value to determine the horizontal dimensions of the structure. This resulted in the mean and minimum/maximum thicknesses as well as the standard deviation of thickness. Fig. 2 (c) shows the

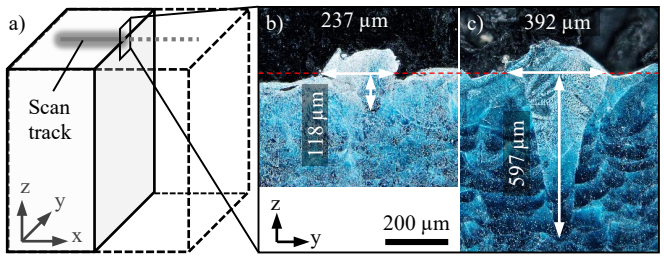


Fig. 1. Schematic representation of the specimens for single track analysis (a) and two exemplary melt pool cross-sections with conduction mode (b) and keyhole mode (c)

results for an example strut with an overhang angle of 50°. For certain evaluations, surface roughness was also considered by using the arithmetic mean $R_a$ of the struts' profile lines, a method also known as center line average (CLA), as described by Volk [29]. In addition, to compare struts with their nominal diameter, the relative error of strut thickness is introduced, which is calculated as follows:

$$relative\ error\ in\ \% = \left(\frac{t_{measured}}{t_{nominal}} - 1\right) \cdot 100 \quad (3)$$

where $t_{measured}$ is the measured average strut thickness and $t_{nominal}$ the nominal designed thickness in the CAD software.

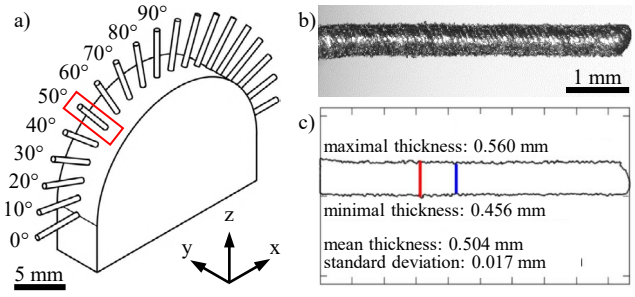


Fig. 2. Example specimen of manufacturing struts (a), microscope image of a strut in the x-z-plane with a build angle of 50° (b), and results of a Matlab analysis of the strut (c, graphically modified)

## 3. Results and discussion

### 3.1. Melt pool characterization

In order to predict the melt pool dimensions, 25 different parameter combinations were used to create single line tracks, as described in Section 2.2. Three cross-sectional micrographs were created from each track to measure width and depth. Thirteen melt pools could not be analyzed, and so the total number of data points was 62. The PBF-LB/M parameters were based on suggestions from Scipioni Bertoli et al. [22]. Accordingly, the laser power was varied between 100 W and 300 W in steps of 50 W, and the scanning speed chosen to limit balling. The resulting parameters for laser power $P_L$ and scan speed $v$ are listed in Table 1. The values and constants listed in Table 2 were used to calculate the normalized enthalpies $\Delta H/h_s$. The initial temperature $T_0$ is assumed to be equal to the nominal build platform temperature of 200 °C.

Fig. 3 shows the results of normalized melt pool depth as a function of normalized enthalpy. Grey circles indicate keyhole mode, while white ones indicate conduction mode. The

Table 1. PBF-LB/M scanning parameters of single line track experiments for melt pool depth and width investigation.

| | Laser power P in W | | | | |
|---|---|---|---|---|---|
| | 100 | 150 | 200 | 250 | 300 |
| Scan velocity v in mm/s | 150 | 225 | 300 | 375 | 450 |
| | 300 | 450 | 600 | 750 | 900 |
| | 385 | 578 | 770 | 963 | 1155 |
| | 550 | 825 | 1100 | 1375 | 1650 |
| | 750 | 1125 | 1500 | 1875 | 1875 |

Table 2. Values and constants used in calculations of normalized enthalpy. *calculated values

| Property | Symbol | Value and Unit | Source |
|---|---|---|---|
| Absorptivity | A | 0.35 | [25] |
| Specific heat capacity | c | 480 J/kg K | [25] |
| Thermal diffusivity | D | $3.93 \cdot 10^{-6}$ m²/s | [25] |
| Enthalpy at melting* | $h_s$ | $4.62 \cdot 10^9$ J/m³ | Eq. (2) |
| Melting temperature | $T_m$ | 1683 K | [25] |
| Density | ρ | 7980 kg/m³ | [23] |
| Beam spot size | σ | 63.7 µm | See: 2.2 |

transition between keyhole and conduction mode is visible and occurs at a normalized enthalpy $\Delta H/h_s$ of roughly 7, as indicated by the dashed vertical line. Following the original paper by Hann et al., the melt pool depth normalized by the spot beam size is scattered as a function of logarithmic normalized enthalpy [24]. A roughly linear dependency of the two melting modes can be observed for the scattered data points. The results of the melt pool depth and width and the linear dependency of the depth were then used to determine the right offset of downskin and filling melt pools using Equation (4). The respective parameters for the constants $m$ and $c$ of the linear fits are given in Table 3:

$$\frac{d}{\sigma} = m\frac{\Delta H}{h_s} + c \quad (4)$$

Despite the manual classification of melt pool geometries using cross-sections being prone to error due to the depth variations shown in the CT scans by King et al., this experiment confirmed the keyhole threshold criterion of $\Delta H/h_s \sim 6$ [22, 23]. Although the value was slightly exceeded, the general scale and shape of the scatter plot were in line with previous findings. The validity of the analysis was thus given, leading to the conclusion that that melt pool approximations should yield

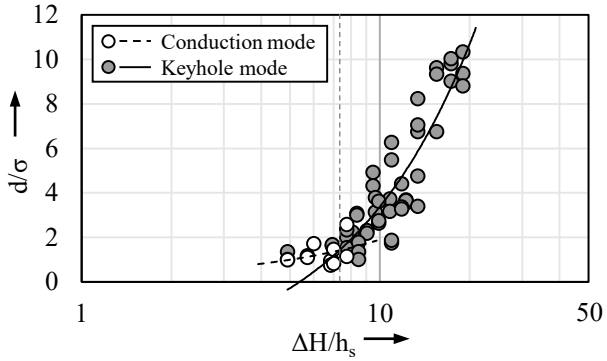


Fig. 3. Semi-logarithmic graph of the melt pool depth normalized by beam size as a function of normalized enthalpy, including linear fit trend lines

robust results. However, in the case of the conduction mode, the low coefficient of determination indicates imprecise prediction. Additional data points are therefore recommended for future applications of this method.

Table 3. Values of the linear fit of normalized enthalpy and normalized melting depth.

| Melting mode | m | c | $R^2$ |
|---|---|---|---|
| Conduction | 0.18 | 0.09 | 12.4 % |
| Keyhole | 0.73 | -3.94 | 81.8 % |
| Total dataset | 44.55 | -223.48 | 83.5 % |

### 3.2. *Strut optimization for build angles of 30°*

The basic principle of the scanning strategy was to align the melt pools such that a pre-melted downskin is able to dissipate the heat from the filing melt pools. Fig. contains a schematic representation of the strategy, with an initially low amount of thermal energy being applied to the loose powder bed (downskin melt pool) before the actual volume scanning (filling melt pool) re-melts a number of previously solidified layers. Alignment of scanning vectors was achieved by setting the *overlap with volume area* for the downskin borders and thus shifting the volume borders, or in this case filling melt pools, away from the part downskin by the amount $l_f$. Sickle-shaped auxiliary geometries on the downskin areas were necessary to achieve the desired filing melt pool offsets for the given data preparation workflow. In order to validate the strategy and set the parameters, a build angle of 30° was initially fixed for the struts, which were built as described in Section 2.2. A velocity of 500 mm/s was set for all scanning vectors. Furthermore, the scanning strategy employed border filling with different parameters for border and filling vectors. The aim was for the downskin melt pool to have an estimated depth of approximately one layer thickness $t$ of 30 µm. An enthalpy $\Delta H/h_s$ of 6 was determined following the linear fit of the normalized enthalpy in keyhole mode right at the threshold value. A laser power of ~ 100 W was calculated with equation (1). To allow for the lower heat conduction in the powder bed compared to the experiment in Section 3.1, the resulting laser power parameters were gradually reduced during the experiment from 100 W down to 40 W in steps of 20 W, representing the minimum enthalpy needed to melt the powder particles (according to the literature) [23]. A minimum downskin melt pool offset $l_{d,0}$ of 80 µm was chosen to account for half the width of the melt pool at given enthalpies. To test for variations in downskin melt pool depth and account for larger melting depths due to increased heat accumulation, the downskin melt pool was shifted away from the strut boundary. Increments were chosen in relation to the molten layer thicknesses and the offset $l_{d,30}$ for one, two and three additional layers, which was calculated as:

$$l_{d,30} = l_{d,0} + \frac{t}{\tan(\alpha)} \tag{5}$$

The downskin offset values examined were thus 80.00, 132, 183 and 236 µm. The parameters of the filling melt pool were selected such that the depth corresponded with approximately three layer thicknesses. A laser power $P_L$ of 125 W and a scan velocity $v$ of 500 mm/s were therefore chosen, corresponding to a normalized enthalpy $\Delta H/h_s$ of 7.50. The filling melt pool offset $l_f$ was set to its default value, which meant that the *overlap with volume area* was zero during this set of experiments.

Fig. 5 shows the results. It can be observed that with the exception of 100 W, an increase in laser power leads to an increase in relative error. This is due to strut thickening as a result of the larger melt pool sizes and the adherence of particles from the powder bed, as was also mentioned in prior research. Furthermore, larger offsets lead to lower relative errors at low laser powers, whereas the opposite is true of high laser powers. A qualitative comparison of the four corner data points is shown in Fig. 6 to illustrate the effects of the offset and of varying the laser power to define the optimum scanning strategy. It can be seen from the horizontal grooves along the lower third of the struts that for a small offset and low laser power, the downskin area of the strut is not fully connected to its main body. In the case of high laser powers with a large offset, too much energy is applied directly into the loose powder bed, which leads to sintering of particles and excess melt. Furthermore, large offsets push the downskin melt pool beyond the filling melt pool, which creates the same effect. However, if the offset and laser power are in balance, it is possible to achieve smooth downskins and high strut fidelity. Although an offset of 80 µm and a laser power of 100 W lead to slightly larger relative errors, struts have a better downskin surface quality of $R_a$ = 26 µm compared to 30 µm for 40 W and

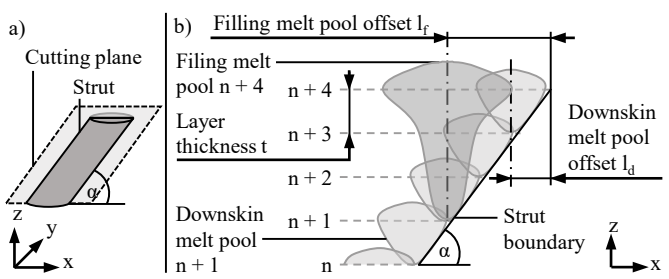


Fig. 4. Strut showing a cutting plane (a) and a schematic illustration of melt pool alignment in a given cutting plane for layers n to n + 4 (b). For enhanced clarity, filling melt pools of layers n to n + 3 are omitted

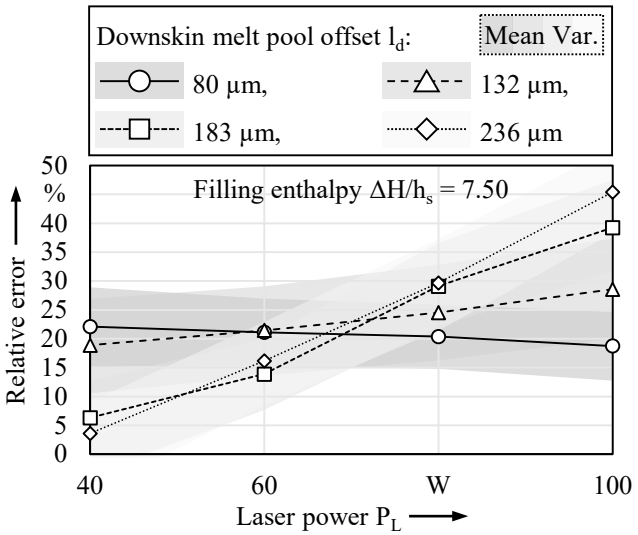


Fig. 5. Relative errors of the strut thickness produced as described in Section 3.2. Width of the grey uncertainty indication in the background shows the mean relative variation (Mean Var.) of the respective measuring point

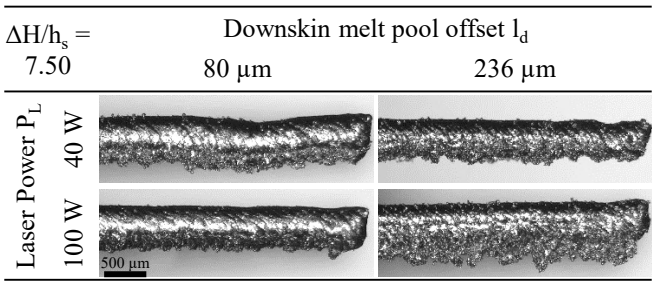


Fig. 6. Optical microscope images of the struts (α = 30°) with the highest and lowest laser power and offsets produced during the experiment described in Section 3.2

an offset of 236 µm, respectively. Thus, the scanning strategy and parametrization derived from the estimated melt pool dimensions (see Section 3.1) yield better results than the other variations examined.

### *3.3. Compensation scheme for build angles of 30° and less*

The results and findings from the previous section were applied to a compensation strategy for 10° and 20°. The downskin scanning parameters were set as shown in the following. Based on the results from Section 3.2, normalized enthalpy $\Delta H/h_s$ was fixed at 6. The previously defined offset $l_{d,0}$ of half the width of the melt pool is not applicable to small build angles due to the aspect ratio of the melt pools. The downskin area is thus shifted along the general length $l_d$, as follows:

$$l_d = \frac{t}{\tan(\alpha)} \tag{6}$$

This enables the downskin melt pool to reach down one effective layer thickness, for the structural bond of consecutive layers. By melting the pre-melted downskin areas with the filling melt pool, which reaches down three effective layer thicknesses based on findings from Section 3.2, excessive heat is conducted along the downskin area, which results in less sintering of particles. The filling area is therefore shifted along the length $l_f$, which is calculated as follows:

$$l_f = \frac{3t}{\tan(\alpha)} \tag{7}$$

As in the procedure from Section 3.2, a full-factorial experiment was conducted with filling laser powers of 80, 90 and 100 W, downskin offset shifts $l_d$ of 15, 30 and 45 µm/tan(α) and build angles of 10, 20 and 30°, to account for variations from melt pool depth measurements and different heat transfers in the powder bed. Fig. 7 shows the results.

As struts with the smallest angles show a large variation in quality (see Fig. 8), the mean relative error is misleading. Thus, in this section, the relative mean variation in thickness of respective struts is used in the analysis. It can be observed that strut thickness variance increases with decreasing build angles for all offsets and laser powers. While the relative mean variation is relatively constant for all laser powers and downskin offsets at build angles of 20° and 30°, strut quality varies at 10°. While some struts with an overhang angle of 10° could not be built, the smallest offset and highest laser power display the lowest relative mean variance, along with high strut uniformity (see Fig. 8). Although considerable thickening occurred with the smallest angle, the scanning strategy led to relative errors that were comparable with previous findings for angles larger than 30° [15]. At 30°, thickening again increases with rising downskin offsets. Downskin roughness. however, was not as strongly influenced by the offset as was the case for lower filling melt pool offsets $l_f$. Comparing the results to previous findings (see Fig. 7), it can be seen that lower shifting values $l_f$ are necessary to perfectly align downskin and filling melt pools. Despite the need for further adjustments, the compensation scheme presented here makes it possible to manufacture struts at small build angles with high uniformity and sufficient fidelity.

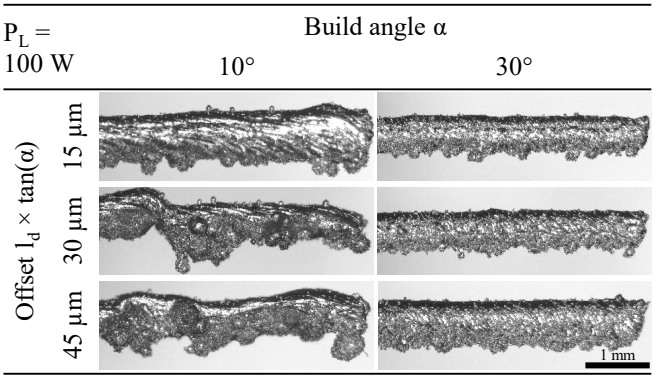


Fig. 8. Optical microscope images of the struts produced using the compensation scheme described in Section 3.2

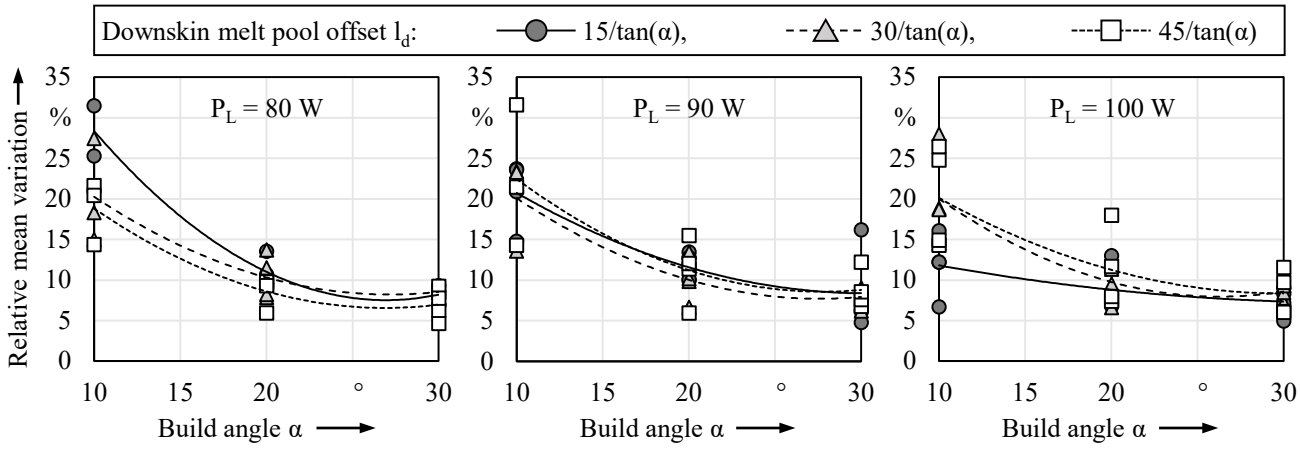


Fig. 7. Relative mean variation of strut thickness for offset shifted melt pools, depending on angle α for different laser powers

## 4. Conclusion and outlook

Further exploitation of the potential of PBF-LB/M for the production of medical implants requires advanced build strategies for complex lattice structures. The low fidelity of thin struts is due to heat accumulation in the powder bed during melting. This study presents a novel approach based on the pre-melting of downskin regions combined with subsequent re-melting of the downskin with a filling melt step. The melt pool positions and dimensions were aligned by way of estimations based on the normalized enthalpy at melting. To sum up the results, the scheme enabled the production of single struts with build angles of 30°, with high dimensional accuracy, smooth surfaces and hardly any sintering of particles. In addition, it was possible to produce struts with a high degree of uniformity and sufficient dimensional accuracy for critical angles down to 10° with respect to the build platform.

Despite these promising results, further work needs to be done to transfer the outlined strategy to industrial applications. This needs to include investigation of a suitable laser power and in turn the melt pool depth for each individual strut angle. Future research should also dive deeper into transferability to different machine systems, and the findings should then be applied to other material systems. Moreover, parameter-based data preparation for angle-dependent build strategies is currently very time-consuming and needs to be simplified.

## Acknowledgements

The authors would like to express their sincere thanks to the German Federal Ministry for Economic Affairs and Energy BMWi for funding the ‘MAIA’ project within its ‘Central Innovation Program for small and medium-sized enterprises’ funding program.

## References

[1] T. Wohlers, R. I. Campbell, R. Huff, O. Diegel, and J. Kowen, Wohlers Report 2019: 3D printing and additive manufacturing: state of the industry. Fort Collins: Wohlers Associates, 2019.

[2] M. F. Zaeh, Wirtschaftliche Fertigung mit Rapid-Technologien: Anwender-Leitfaden zur Auswahl geeigneter Verfahren, 1st ed. Munich: Hanser, 2013.

[3] I. Gibson, D. Rosen, and B. Stucker, Additive manufacturing technologies: 3D printing, rapid prototyping and direct digital manufacturing. New York, Heidelberg, Dodrecht, London: Springer, 2015.

[4] B. Schramm et al., “Medizintechnische Anwendungen der additiven Fertigung,” in Additive Fertigung von Bauteilen und Strukturen, H. A. Richard, B. Schramm, and T. Zipsner, Eds., Wiesbaden: Springer Vieweg, 2017, pp. 21–40.

[5] X. P. Tan, Y. J. Tan, C.S.L. Chow, S. B. Tor, and W. Y. Yeong, “Metallic powder-bed based 3D printing of cellular scaffolds for orthopaedic implants: A state-of-the-art review on manufacturing, topological design, mechanical properties and biocompatibility,” Materials Science and Engineering: C, vol. 76, pp. 1328–1343, 2017.

[6] S. Arabnejad, J. R. Burnett, J. A. Pura, B. Singh, M. Tanzer, and D. Pasini, “High-strength porous biomaterials for bone replacement: A strategy to assess the interplay between cell morphology, mechanical properties, bone ingrowth and manufacturing constraints,” Acta biomaterialia, vol. 30, 2016.

[7] E. Wintermantel and S.-W. Ha, Medizintechnik: Life Science Engineering; Interdisziplinarität, Biokompatibilität, Technologien, Implantate, Diagnostik, Werkstoffe, Zertifizierung, Business, 5th ed, Berlin and Heidelberg: Springer, 2009.

[8] W. Tao and M. C. Leu, “Design of lattice structure for additive manufacturing,” in International Symposium on Flexible Automation: ISFA 2016, Cleveland, OH, USA, 2016, pp. 325–332.

[9] E. Liverani et al., “Fabrication of Co–Cr–Mo endoprosthetic ankle devices by means of Selective Laser Melting (SLM),” Materials & Design, vol. 106, pp. 60–68, 2016.

[10] M. Tilton, G. S. Lewis, and G. P. Manogharan, “Additive Manufacturing of Orthopedic Implants,” in Orthopedic Biomaterials: Progress in Biology, Manufacturing, and Industry Perspectives, B. Li and T. Webster, Eds., Cham: Springer International Publishing, 2018, pp. 21–55.

[11] L. Yuan, S. Ding, and C. Wen, “Additive manufacturing technology for porous metal implant applications and triple minimal surface structures: A review,” Bioactive Materials, vol. 4, pp. 56–70, 2019.

[12] L. Bai et al., “Additive Manufacturing of Customized Metallic Orthopedic Implants: Materials, Structures, and Surface Modifications,” Metals, vol. 9, no. 9, p. 1004, 2019.

[13] M. Maniruzzaman, 3D and 4D Printing in Biomedical Applications: Process Engineering and Additive Manufacturing. Newark: John Wiley & Sons Incorporated, 2018.

[14] Z. S. Bagheri, D. Melancon, L. Liu, R. B. Johnston, and D. Pasini, “Compensation strategy to reduce geometry and mechanics mismatches in porous biomaterials built with Selective Laser Melting,” Journal of the Mechanical Behavior of Biomedical Materials, vol. 70, pp. 17–27, 2017.

[15] DIN EN ISO/ASTM 52911-1:2020-05, Additive manufacturing - Design - Part 1: Laser-based powder bed fusion of metals, Berlin: Beuth.

[16] G. Li et al., “In vitro and in vivo study of additive manufactured porous Ti6Al4V scaffolds for repairing bone defects,” Scientific reports, vol. 6, p. 34072, 2016.

[17] R. Vrána et al., “Selective Laser Melting Strategy for Fabrication of Thin Struts Usable in Lattice Structures,” Materials, vol. 11, no. 9, p. 1763, 2018.

[18] Y. Tian, D. Tomus, P. Rometsch, and X. Wu, “Influences of processing parameters on surface roughness of Hastelloy X produced by selective laser melting,” Additive Manufacturing, vol. 13, pp. 103–112, 2017.

[19] T. Gustmann et al., “Properties of a superelastic NiTi shape memory alloy using laser powder bed fusion and adaptive scanning strategies,” Prog Addit Manuf, vol. 5, no. 1, pp. 11–18, 2020.

[20] M. Illgner, M. Binder, G. Schlick, C. Seidel, and G. Reinhart, “Laser Beam Melting of Complexly Shaped Honeycomb Structures,” TLS, vol. 1, no. 2, 2018.

[21] W. Meiners, “Direktes selektives Laser Sintern einkomponentiger metallischer Werkstoffe,” Dissertation, Aachen, 1999.

[22] U. Scipioni Bertoli, A. J. Wolfer, M. J. Matthews, J.-P. R. Delplanque, and J. M. Schoenung, “On the limitations of Volumetric Energy Density as a design parameter for Selective Laser Melting,” Materials & Design, vol. 113, pp. 331–340, 2017.

[23] W. E. King et al., “Observation of keyhole-mode laser melting in laser powder-bed fusion additive manufacturing,” Journal of Materials Processing Technology, vol. 214, no. 12, pp. 2915–2925, 2014.

[24] D. B. Hann, J. Iammi, and J. Folkes, “A simple methodology for predicting laser-weld properties from material and laser parameters,” Journal of Physics D: Applied Physics, vol. 44, no. 44, p. 445401, 2011.

[25] J. Metelkova, Y. Kinds, K. Kempen, C. de Formanoir, A. Witvrouw, and B. van Hooreweder, “On the influence of laser defocusing in Selective Laser Melting of 316L,” Additive Manufacturing, vol. 23, pp. 161–169, 2018.

[26] M. Marcolongo, S. Sarkar, and N. Ganesh, “Trends in Materials for Spine Surgery,” in Comprehensive Biomaterials II, P. Ducheyne, K. Healy, D. E. Hutmacher, D. W. Grainger, and C. J. Kirkpatrick, Eds., Saint Louis: Elsevier Science, 2017, pp. 175–198.

[27] ISO 13320:2009-10 - Particle size analysis - Laser diffraction methods, Berlin: Beuth.

[28] DIN EN ISO 11146-2:2005-05, Lasers and laser-related equipment - Test methods for laser beam widths, divergence angles and beam propagation ratios - Part 2: General astigmatic beams, German version, Berlin: Beuth.

[29] R. Volk, Rauheitsmessung: Theorie und Praxis, 3rd ed. Berlin, Wien, Zürich: Beuth, 2018.